ACSNANO

www.acsnano.org

ARTICLE

# Glutamine Antagonist Synergizes with Electrodynamic Therapy to Induce Tumor Regression and Systemic Antitumor Immunity

Gui Chen,[‖] Qing Xu,[‖] Zhenzhen Feng, Qinqin Xu, Xuhui Zhang, Yuanyuan Yang, Yuxuan Zhang, Xing-Jie Liang,* Zhiqiang Yu,* and Meng Yu*

Cite This: https://doi.org/10.1021/acsnano.1c08544

Read Online

ACCESS | Metrics & More | Article Recommendations | Supporting Information

**ABSTRACT:** Electrodynamic therapy (EDT) combining nanotechnology with electronic current was used in this study to generate highly cytotoxic oxidative hydroxyl radicals (·OH) for tumor destruction. However, increasing evidence suggests that EDT treatment alone for one time still faces great challenges in achieving long-term tumor suppression in an immunosuppressive environment, which would raise the risk of later tumor recurrence. Benefitting from the marvelous potential of reactive oxygen species (ROS)-mediated dynamic therapies in tumor immunocombination therapy due to their immunogenic cell death (ICD) effect, a glutamine antagonist 6-diazo-5-oxo-L-norleucine (DON)-loaded nanocarrier (Pt−Pd@DON) was designed for combination therapy (EDT and immunotherapy) against tumor recurrence and metastasis. The protective immune response was motivated in highly immunosuppressive tumors by the joint functions of ICD and $CD8^+$ T cell infiltration promoted by DON. A great therapeutic efficacy has been demonstrated in primary and metastatic tumor models, respectively. This study has provided an effective thought way for clinical highly immunosuppressive tumor treatment.

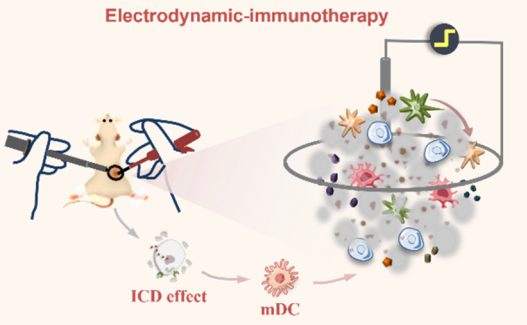


**KEYWORDS:** *electrodynamic therapy, reactive oxygen species, immunogenic cell death, glutamine antagonists, immunotherapy*



In recent years, reactive oxygen (ROS)-amplified tumor therapy that can regulate the mitochondria redox metabolism[1,2] and cause damage of the fundamental lipids, proteins, and DNA[3,4] has shown marvelous potential to induce tumor regression. An increasing number of strategies have been developed to attack tumor cells by promoting intracellular ROS production, e.g., photodynamic therapy (PDT),[5] chemodynamic therapy (CDT),[6] chemophotodynamic therapy (C-PDT),[7] sonodynamic therapy (SDT),[8] radiotherapy (RT),[9] and radiodynamic therapy (RDT).[10] However, there are various obstacles hindering the clinical development of the above strategies, such as the short penetration depth of light in PDT, the insufficient endogenous $H_2O_2$ of CDT, and the expense of damage to the surrounding tissues during RT. Therefore, an electrodynamic therapy (EDT) combining nanotechnology with electronic current has emerged to realize efficient cancer therapy *via* enhancing "combination-dynamic therapies".[11] Once triggered by an external electric field, nanomaterials depending on specific metal or composite metals with large catalyst surface areas are more conducive to generate highly oxidative ROS (hydroxyl radicals, ·OH) without the presence of endogenous $H_2O_2$ or $O_2$. These metal-based nanomaterials in EDT are considered to have good biological safety and will not cause damage to the surrounding tissues or lead to systemic side effects.[12] Moreover, electrode stimulation is like an interventional strategy that facilitates therapy against deep-seated tumors and also benefits the elimination of large-sized tumors. Therefore, EDT shows effective tumor destruction advantages in clinical use for its feasibility in remotely controlled electric field and low side effects. Although the sole use of EDT with a therapeutic process for only a dozen minutes or less can achieve great tumor ablation effect, there are still great challenges in achieving long-term tumor suppression after a

Received: September 28, 2021
Accepted: December 30, 2021

**Scheme 1. Schematic Illustration of an Advanced Antitumor Platform of Metallic Nanoflowers Carrying Glutamine Antagonist DON (Pt−Pd@DON)**[a]

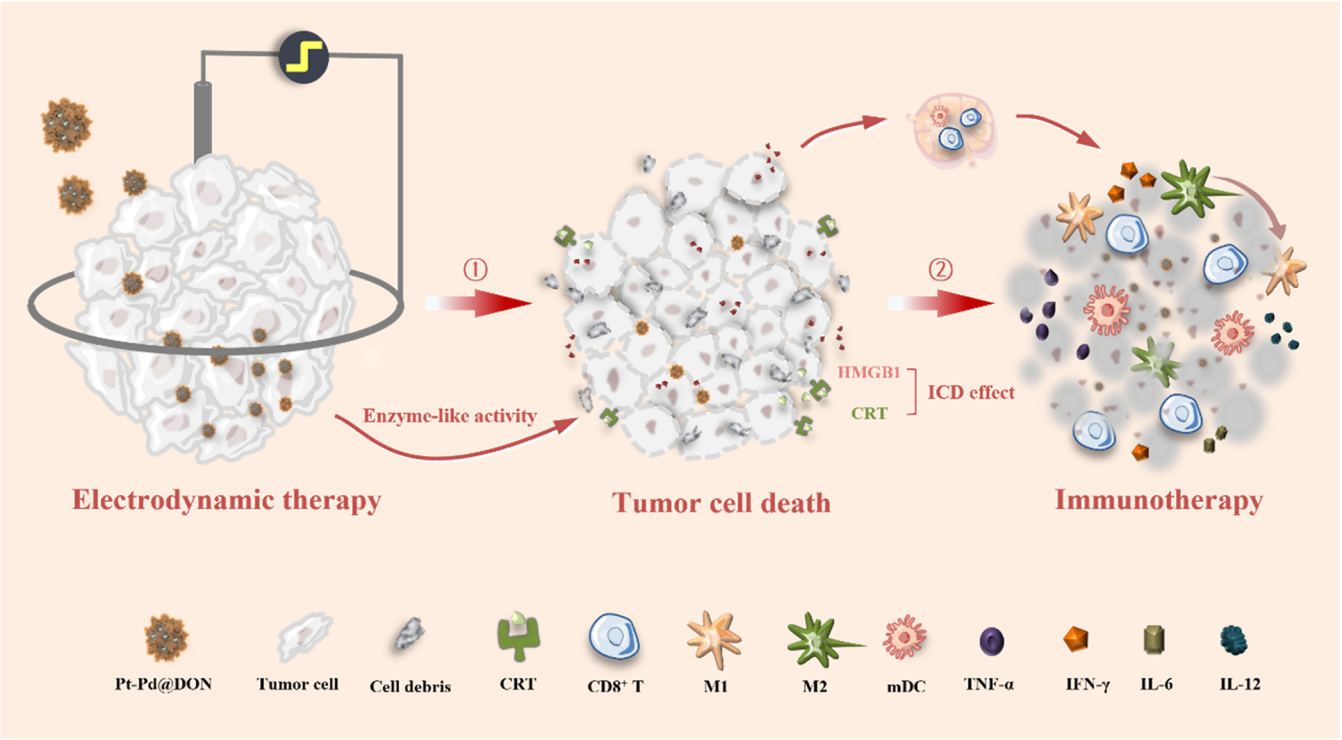


[a]The platform was designed for electrodynamic immune therapy. First, Pt−Pd@DON directly displayed tumor ablation effect through EDT. Second, EDT-evoked the ICD effect, and DON reshaped the tumor immune microenvironment for synergistic immunotherapy by increasing $CD8^+$ T cells infiltration, promoting M2 macrophages polarization, and improving DCs maturation.

single EDT treatment,[13−15] which would raise the risk of later tumor recurrence.

Numerous researches have proved that "dynamic therapies" bring out great potential in immune adjuvant therapies attributing to their accompanied immunogenic cell death (ICD). The apoptotic/necrotic tumor cells during ICD would actively or passively release cell death associated molecular patterns (DAMPs) to reverse the immunosuppressive tumor microenvironment, ultimately remodeling the "cold" tumor into "hot" tumor.[16−18] In other words, the ICD effect could evoke tumor immunogenicity by DAMPs, thereafter promoting dendritic cells (DCs) maturation and then further recruiting and activating tumor cytotoxic T cells ($CD8^+$ T cells) to engulf the residual tumor cells.[19,20] Notably, unlike ROS generation in water electrolysis, EDT produces ·OH catalyzed by metal materials under the square-wave current and consequently displays direct tumor killing activity and an accompanying ICD effect. Inspired by the above concepts, we have rationally hypothesized that EDT showed a promising application in immunoadjuvant therapies due to the ICD-evoking potential.

Increasing research has combined EDT with other therapies, such as starvation treatment[21] and chemotherapy[22] against tumor recurrence risk. However, EDT-related combined therapeutic strategies still urgently need improvements to prevent tumor metastasis and recurrence caused by long-term tumor suppression after a single treatment of EDT. Aiming to achieving these goals, immunotherapies depending on immune-checkpoint-blocking antibodies,[23] small-molecule drugs,[24] or cytokines[25] have been jointly used with traditional antitumor therapies including "dynamic therapies", chemotherapy and photothermal therapy.[26] Benefitting from the ICD effect of EDT, small-molecule immune adjuvants have been applied for joint immunotherapy.[27,28] The small-molecule glutamine antagonist 6-diazo-5-oxo-L-norleucine (DON) is reported to inhibit a broad range of glutamine-requiring enzymes,[29,30] thus leading to potent inhibition of viability,[31] self-renewal, and metabolism of tumor cells.[32] Convincing clinical evidence has confirmed that DON was an effective immune adjuvant to treat highly immunosuppressive tumors due to its promoting effects on $CD8^+$ T cell infiltration through extensive reduction of hyaluronan and collagen in the tumor microenvironment.[33] In addition, DON would also protect ROS produced in EDT from being eliminated by preventing glutathione production.

Therefore, we rationally designed an advanced therapeutic platform to incorporate porous Pt−Pd nanoflowers (Pt−Pd NFs) with DON (Pt−Pd@DON) for synergistic electrodynamic immunotherapy (Scheme 1). DON can prevent the production of glutathione and avoid the elimination of ROS under electric field to kill tumor cells accompanied by an excellent ICD effect, which subsequently elicited a *in vivo* protective immune response for long-term tumor suppression. Meanwhile, Pt−Pd NFs were able to assist DON in enhancing DCs maturation and $CD8^+$ T cells infiltration by hypoxia relief under endogenous $H_2O_2$ conditions. Significant *in vitro* and *in vivo* antitumor effect was achieved by EDT in combination with glutamine metabolism inhibition, achieving the great effect of preventing recurrence and metastasis *via* inspiring protective immunity. Consequently, this work employs a strategy combining EDT with immunotherapy to realize the total ablation of solid tumor without limitation by endogenous


https://doi.org/10.1021/acsnano.1c08544
ACS Nano XXXX, XXX, XXX−XXX

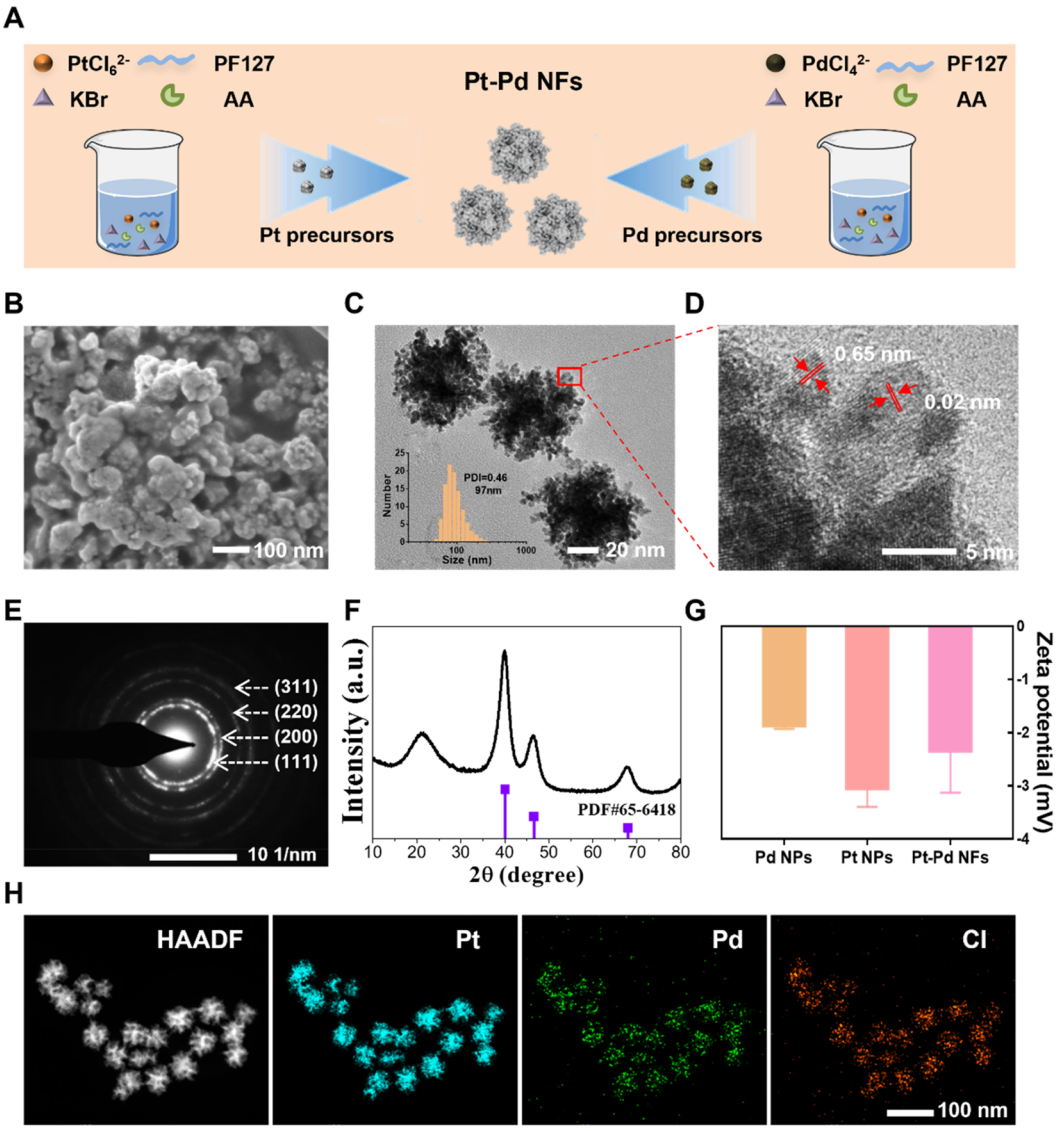


**Figure 1. Characterization of Pt−Pd NFs. (A) Schematic illustration of the formation of Pt−Pd NFs. (B) SEM image. (C, inset: DLS data) TEM image. (D) High-resolution TEM image of Pt−Pd NFs. (E) SAED and (F) XRD patterns of Pt−Pd NFs. (G) Zeta potentials of Pt NPs, Pd NPs, and Pt−Pd NFs. (H) STEM element mapping of Pt−Pd NFs.**

energy, meanwhile inhibiting tumor metastasis and preventing tumor relapse.

## RESULTS AND DISCUSSION

The preparation method of Pt−Pd NFs was optimized from the metallic complexes synthesis reported in previous studies (Figure 1A).[21] Pt and Pd precursors (Pt and Pd NPs) were synthesized according to a one-step chemical reaction by reducing $H_2PtCl_6$/$Na_2PdCl_4$ with ascorbic acid in the presence of Pluronic F127 and KBr. The precursor mixture was incubated overnight to obtain Pt−Pd NFs. The well-dispersed Pt−Pd NFs showed uniform and sphere-branched structures with a dimension of 97 nm (Figures 1B,C and S1). The Pt−Pd NFs were assembled by nanocrystals with sizes between 0.02 and 0.65 nm under observation *via* high-resolution transmission electron microscopy (HRTEM) (Figure 1D), facilitating the catalytic activity due to the large surface area and high population of exposed superficial sites of branched structures. The corresponding selected-area electron diffraction (SAED) pattern with concentric rings and bright spots indicated the polycrystalline characters of Pt−Pd NFs (Figure 1E). The polycrystalline structure of Pt−Pd NFs was further evidenced by the X-ray diffraction (XRD) pattern (Figure 1F), which was consistent with the results of the SAED pattern. The element mapping from scanning transmission electron microscopy (STEM) results showed that the Pt, Pd, and Cl were uniformly distributed in Pt−Pd NFs (Figure 1H and S2), further validated the success construction of the nanostructure. The weak negative surficial $\zeta$ potential of Pt−Pd NFs made them barely be driven to move under an electric field (E), facilitating their stability in physiological circumstances as well as avoiding a large charge gradient during the treatment (Figures 1G and S3). The UV−vis absorption spectra of Pt−Pd NFs exhibited a concentration-dependent absorption at 808 nm, which was not an obvious difference from that of Pt NPs (Figure S4).

The electro-driven catalytic performance of Pt−Pd NFs was evaluated by methylene blue (MB), which would show a decreased absorption at 664 nm under ROS generation. As shown in Figure 2A, a double salt bridge system was equipped


https://doi.org/10.1021/acsnano.1c08544
ACS Nano XXXX, XXX, XXX−XXX

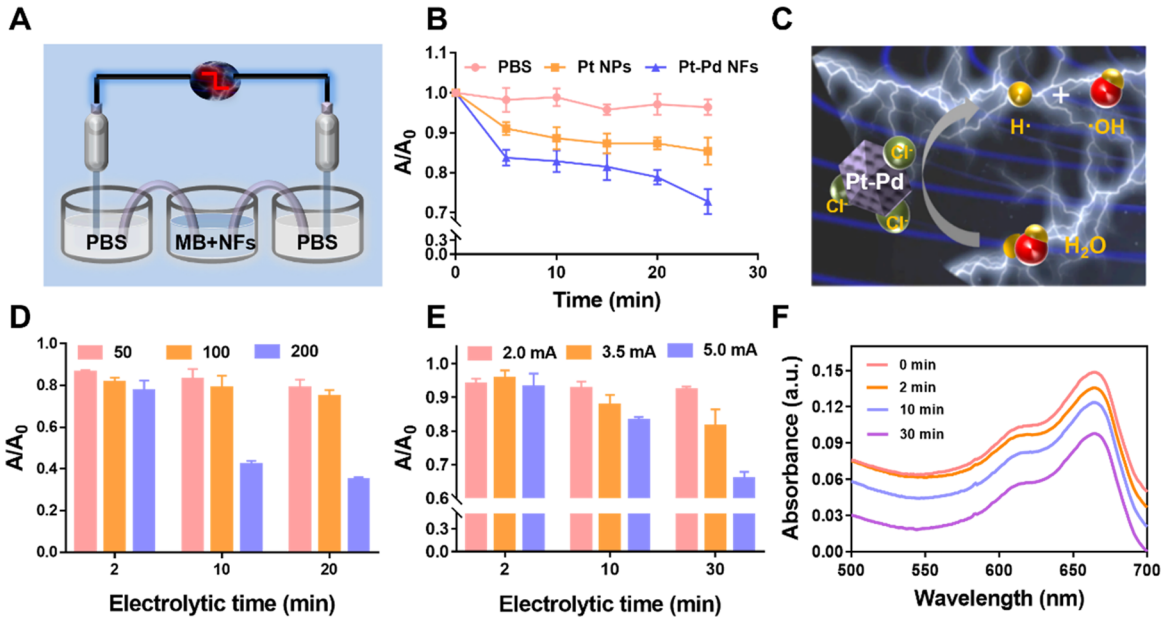


**Figure 2. Electro-driven catalytic performance. (A) Schematic illustration of the equipment for electro-driven catalytic experiment. (B) Degradation rates of MB in various solutions (Pt: 50 μg/mL). (C) Mechanism illustration of EDT treatment. Electro-driven catalytic performance evaluated by the degradation of MB (D) under different Pt−Pd NFs concentrations (Pt: 50, 100, and 200 μg/mL) and (E) different current intensities. (F) UV−vis absorption spectra of MB in Pt−Pd NFs (100 μg/mL) solutions under 100 s of 5 mA square-wave AC.**

to investigate the electrocatalytic activity of Pt−Pd NFs. The absorption of MB (at 664 nm) was decreased due to the presence of ·OH generated *via* catalysis by Pt and Pd ions under a square-wave alternating current (AC). In comparison with the restricted effect of solely metal-additive nanomaterials (Pt NPs), the composite metal nanoparticles Pt−Pd NFs showed significantly reduced the MB level under the EDT with 10 mHz square-wave electric signal output (Figures 2B and S5), implying that the additional metal component in composite metal nanoparticles (Pt−Pd NFs) could perform synergistic catalytic effects with Pt. Different from electrolysis of water that $H^+$ and $OH^-$ undergo oxidation−reduction reaction, electronic exchanges in EDT took place between $H_2O$ molecules and surface of Pt−Pd NFs due to participation of chloride ions in solutions and thus generated ·OH without an obvious pH gradient (Figure 2C).[11] The highly exposed superficial sites and high concentration of nanoparticles as well as the strong electric field that activates the electron/charge motion together facilitated the catalytic activity.[22] Hence, the catalysis behaviors of the nanoflowers were further investigated at different conditions. The electrocatalytic activity of Pt−Pd NFs was rapidly improved along with the increase of metal concentration, electric current, and electrolysis time (Figure 2D−F, S6, and S7).

To further validate the electro-driven EDT effect, the cellular uptake of Pt−Pd NFs by 4T1 breast tumor cells was investigated using confocal laser scanning microscopy (CLSM) and flow cytometry (Figure S8). The Pt−Pd NFs showed quick and time-dependent internalization behavior by 4T1 cells. RhB-labeled Pt−Pd NFs have been found to colocalize with the fluorescence signal of lysosomes, suggesting the efficient cellular uptake of Pt−Pd NFs through the lysosome pathway, which was mainly due to their multibranched nanoparticle structure. No significant cytotoxicity to 4T1 cells was observed after incubation with both Pt nanoparticles and Pt−Pd NFs (even at a metal concentration up to 100 μg/mL), suggesting the good *in vitro* biocompatibility of these metal nanoparticles (Figure 3A). Thereafter, to eliminate the interference of water electrolysis that only generated ROS near the electrodes, a double salt bridge system was equipped to investigate the electrocatalytic activity of Pt−Pd NFs during the EDT effect by detecting the ROS generation in the middle chamber. As shown in Figure 3B, Pt−Pd NFs exhibited a cytotoxicity to 4T1 cells that was significantly higher than that of Pt NPs under stimulation by electric field. Obviously, the cytotoxicity of Pt−Pd NFs was enhanced along with the increase of metal concentration, electrolysis time, and square-wave AC intensity, further verifying that the electrocatalytic activity of Pt−Pd NFs could be flexibly adjusted by optimizing the parameters (Figure 3C). One of the supervirulent ROS, ·OH, is a vital messenger molecule during EDT-related tumor cell death. An ROS probe, 2′,7′-dichlorofluorescin diacetate (DCFHDA), was used to evaluate intracellular ROS production by CLSM observation and flow cytometry analysis (Figure 3D,E). No clear fluorescence was presented in the tumor cells incubated with Pt NPs, while limited ROS signal was displayed after cells were treated with Pt−Pd NFs. Elevated levels of ROS intensity were detected in 4T1 cells after providing an electric field (E). Obviously, Pt−Pd NFs+E induced more significant intracellular ROS than that of Pt NPs +E to kill tumor cells due to the additional Pd element. It is noteworthy that the electric field itself did not produce an obvious ROS signal, further confirming that ROS generation in EDT was highly dependent on chlorine adsorption and water dissociation rather than the direct electrolysis of water. ROS production is often accompanied by a decrease of mitochondrial membrane potential (MMP),[34,35] which would lead to JC-1 fluorescent probe monomers (green fluorescence) being unable to enter the matrix of inactive mitochondrion to form aggregates (red fluorescence). Thus, the lowest red/green ratio of JC-1 fluorescent dyes in Pt−Pd NFs+E group indicated the


https://doi.org/10.1021/acsnano.1c08544
ACS Nano XXXX, XXX, XXX−XXX

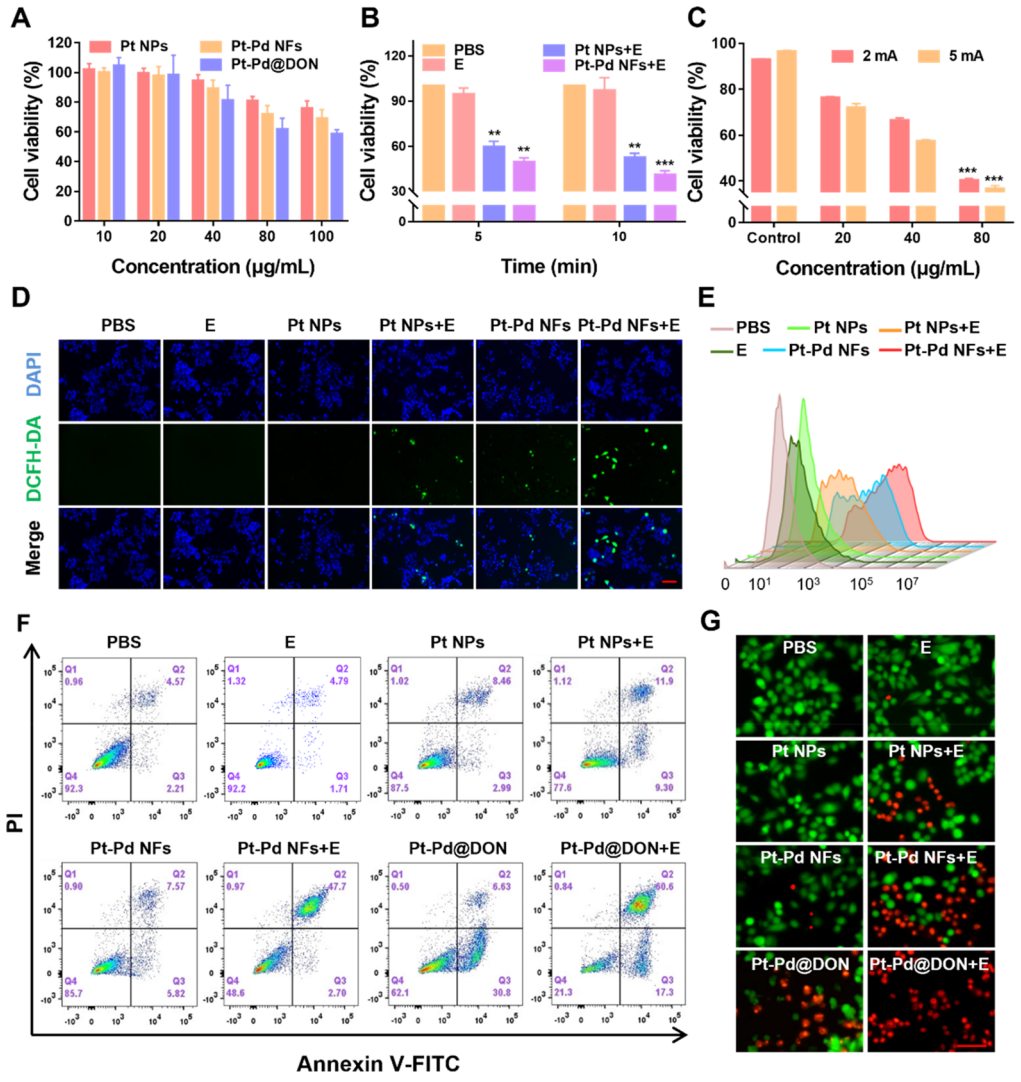


**Figure 3.** ***In vitro*** **EDT effect and cytotoxicity. (A) Relative cell viabilities of 4T1 cells after incubation with various formulations for 24 h at different concentrations. (B) Relative cell viability of electrodynamic-treated 4T1 cells after incubation with different formulations under square-wave AC (10 mHz, 5 mA) for 5 or 10 min. (C) Relative cell viability of 4T1 cells after incubation with Pt−Pd NFs under different electro-driven currents. Intracellular ROS production in 4T1 cells after different treatments with/without electric stimulation detected by (D) CLSM and (E) flow cytometer. Scale bar: 100 $\mu$m. (F) Cell apoptosis of 4T1 cells 24 h post EDT treatment with different formulations. (G) Calcein-AM/PI staining of electrodynamic-suffered 4T1 cells treated with various formulations. Scale bar: 100 $\mu$m. *, $P < 0.05$, **, $P < 0.01$, and ***, $P < 0.001$.**

greatest mitochondrial depolarization and the strongest tumor cell cytotoxicity (Figure S9).

It has been reported that ROS-mediated dynamic therapies are insufficient to activate systemic immunity against tumor metastasis in immunosuppressive microenvironment.[36,37] DON has been applied as an immune adjuvant to promote $CD8^+$ T cell infiltration for eliciting systemic protective immunity.[38] In addition, DON was also used as a glutamine antagonist that disrupts the metabolic balance in tumors *via* inhibition of the hexosamide pathway to protect EDT-induced ROS from being eliminated. Inspired by the antitumor potential of intracellular oxidative stress increase and MMP dissipation, the synergistic antitumor effect of Pt−Pd NFs carrying metabolism inhibitor DON (Pt−Pd@DON) was further investigated in 4T1 cells by cell apoptosis and the live/dead staining experiments. Pt−Pd@DON resulted in 30.8% early apoptosis due to the presence of lethal DON; meanwhile, Pt−Pd NFs caused almost no early apoptosis of 4T1 cells. In addition, cell apoptosis was increased up to approximately 80% once an electric field was provided (Pt−Pd@DON+E; Figure 3F). The results of live/dead double staining experiments also revealed an excellent tumor cell killing effect of Pt−Pd@DON +E (Figure 3G).

ICD is considered a special form of apoptosis that can release related antigens including apoptosis bodies, damage DNA fragments, and helps hosts with competent immunity to trigger a specific immune response.[39] It has been reported that "combination-dynamic therapies" are capable of eliciting the ICD effect *via* triggering dying tumor cells to express DAMPs, including the endoplasmic reticulum chaperones calreticulin (CRT), adenosine triphosphate (ATP), and high mobility group box 1 (HMGB1). Subsequently, antigen-presenting cells (APCs) including DCs would be activated to present tumor antigens and finally stimulate immune responses against tumors (Figure 4A). As expected, the significant CRT exposure on the cellular surface and HMGB1 reduction inside the


https://doi.org/10.1021/acsnano.1c08544
ACS Nano XXXX, XXX, XXX−XXX

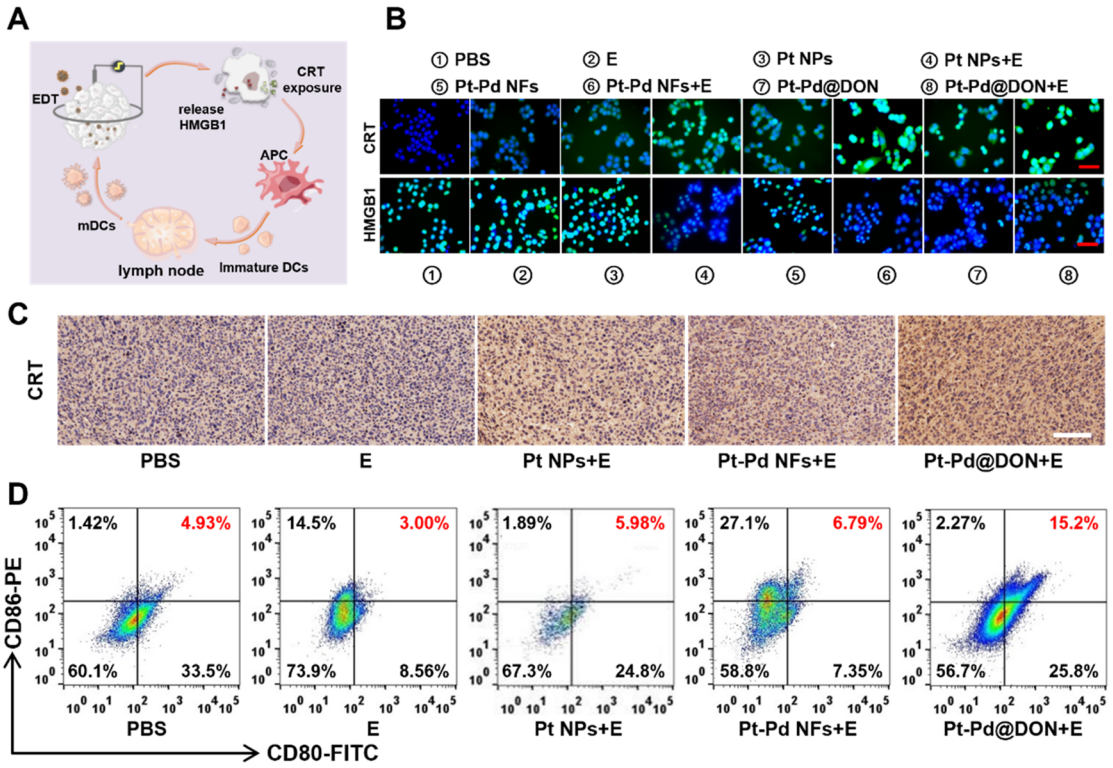


**Figure 4.** *In vitro* and *in vivo* EDT-induced ICD effect. (A) Schematic illustration of synergistic immune responses in tumor tissue triggered by Pt−Pd NFs and EDT-induced ICD effect. (B) CLSM images of CRT exposure and HMGB1 release of 4T1 cells. Scale bar: 100 $\mu$m. (C) Immunohistochemical analysis for *in situ* CRT exposure in 4T1 tumors from mice after various treatments. Scale bar: 100 $\mu$m. (D) Flow cytometry examination of tumor draining lymph node cells collected from 4T1 tumor-bearing mice for *in vivo* DC maturation.

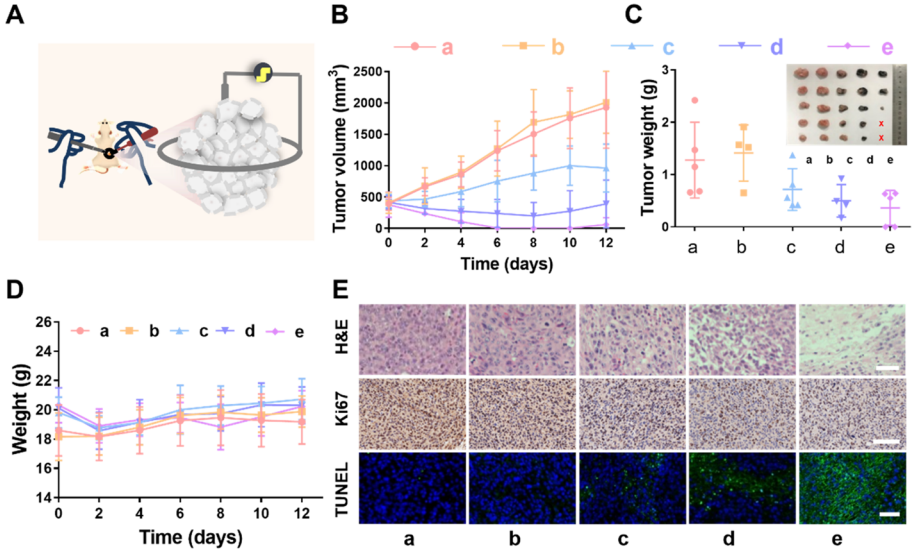


**Figure 5.** *In vivo* synergetic antitumor performance of EDT and DON inhibitor. (A) The schedule of synergistic treatment studies. The 4T1 tumor-bearing mice were intratumorally injected with PBS, Pt NPs, Pt−Pd NFs, and Pt−Pd@DON, and then treated with square-wave AC power (5 mA, 5 min). (B) Tumor growth curves, (C) average tumor weights (inset: photographs of tumors), and (D) body weights of 4T1 tumor-bearing mice after different treatments ($n$ = 5). (E) H&E (scale bar: 50 $\mu$m), Ki67 (scale bar: 100 $\mu$m) and TUNEL (scale bar: 50 $\mu$m) stained tumor slices collected from different groups after treatment. (a) PBS, (b) E, (c) Pt NPs+E, (d) Pt−Pd NFs+E, and (e) Pt−Pd@DON +E.

nucleus were observed in the Pt NPs+E, Pt−Pd NFs+E, and Pt−Pd@DON+E groups compared with the PBS-treated group, which fully proved the ability of EDT to induce an ICD effect (Figure 4B). Inspired by the excellent ICD effect *in vitro*, expression of intratumoral CRT and HMGB1 *in vivo* was further characterized on 4T1 tumor-bearing mice. Increased CRT expression and prominent HMGB1 migration from nucleus to cytoplasm was observed in tumors from 4T1 tumor-bearing mice after EDT treatments (Pt NPs+E, Pt−Pd NFs+E, and Pt−Pd@DON+E), evidencing the efficient ICD potential


https://doi.org/10.1021/acsnano.1c08544
ACS Nano XXXX, XXX, XXX−XXX

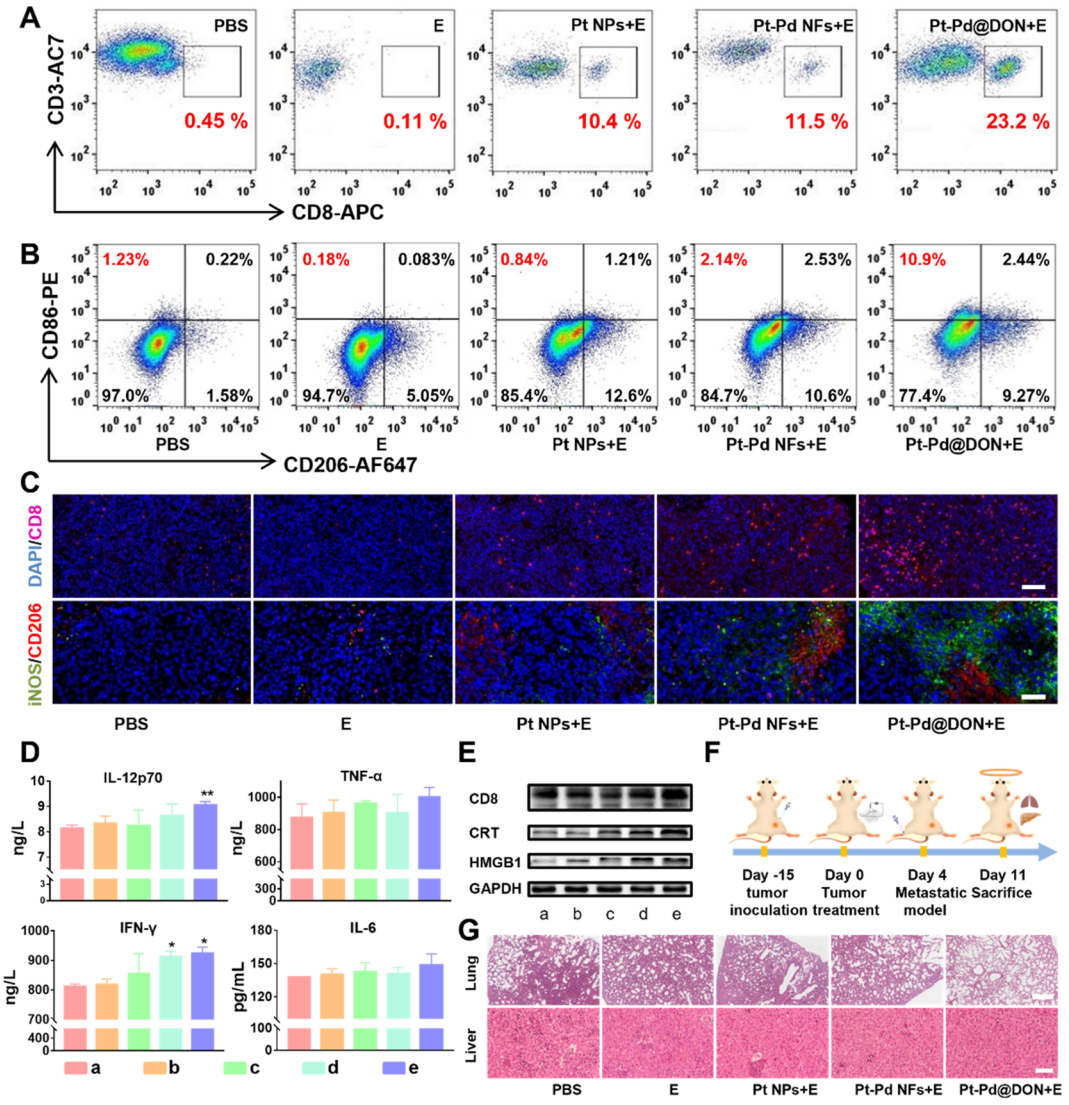


**Figure 6. Immune mechanism evaluation of Pt−Pd@DON+E-mediated synergistic antitumor effects. (A) Representative flow cytometry plots showing $CD3^+CD8^+$ T cell ratios in tumor tissues after different treatments. (B) Flow cytometric analysis of the single cells in tumors of each treatment group stained with CD45, CD11b, F4/80, CD86, and CD206. (C) Immunofluorescence analysis of CD8 expression (scale bar: 100 μm), and tumor-associated macrophages (scale bar: 50 μm). iNOS and CD206 were used as markers for the M1 and M2 phenotypes, respectively. (D) ELISA analysis of cytokines in serum from 4T1 tumor-bearing mice, including IL-12p70, TNF-α, IFN-γ, and IL-6 ($n$ = 3). (E) Western blot analysis of relevant proteins in tumor tissues after different treatments. (a) PBS, (b) E, (c) Pt NPs+E, (d) Pt−Pd NFs+E, and (e) Pt−Pd@DON+E. (F) Schematic illustration of tumor metastasis model construction and therapeutic schedule. (G) H&E staining of lungs (scale bar: 500 μm) and livers (scale bar: 10 μm) harvested from 4T1-bearing mice injected with cell suspension intravenously at 11 days after treatment. *, $P < 0.05$, **, $P < 0.01$, and ***, $P < 0.001$.**

of EDT-dependent therapies (Figures 4C and S10). In addition, release of HMGB1 acted as a "find me" signal, while exposure of CRT acted as an "eat me" signal, which are essential to accelerate the maturation of immature DCs in tumor tissues.[23] As presented in Figure 4D, the proportion of mature DCs (mDCs) is as high as 15.2% in the Pt−Pd@DON +E group, which was 3-fold more than that of PBS in tumor-draining lymph nodes collected from 4T1 tumor-bearing mice. However, the Pt NPs+E and Pt−Pd NFs+E groups only showed slight DCs maturation due to low immunogenicity in immune-suppressive tumors. The above results indicate that Pt−Pd@DON+E can effectively promote the maturation of DCs owing to the coworking of the ICD effect by EDT and immunosuppression conversion by DON, thereby activating a strong protective immune response against the tumor challenge.

When the tumor volumes grew to about 500 $mm^3$, 4T1 tumor-bearing mice were randomly divided into 5 groups (PBS, E, Pt NPs+E, Pt−Pd NFs+E, and Pt−Pd@DON+E, $n$ = 5 in each group) and received intratumoral injections of different solutions with/without square-wave AC power treatment for 5 min (Figures 5A and S11). Tumor volumes and body weights were recorded during treatments. It was found that the Pt−Pd NFs+E group showed more effective tumor growth suppression than did the Pt NPs+E group, evidencing that the additional metal ion component in the composite metal nanoparticles could carry out synergistic EDT for tumor killing. When the mice were treated with Pt−Pd@DON+E, tumors almost completely disappeared (Figure 5B).


https://doi.org/10.1021/acsnano.1c08544
ACS Nano XXXX, XXX, XXX−XXX

Moreover, the 4T1 cells were subcutaneously injected to construct a distant tumor at 3 days after primary tumors were ablated in the tumor cell challenge experiment. As demonstrated, the primary tumors gradually collapsed after treatment by EDT combined with DON and were totally ablated at 12 days. More importantly, the distant tumors constructed by tumor cell challenge measure were unsuccessfully colonized. In contrast, the tumor-cutting experiment was carried out by incompletely cutting out the solid tumor tissues. EDT with DON was applied for postsurgery treatment against the residual tumor tissue (~200 $mm^3$). Tumor growth was completely inhibited and showed no recurrence (Figure S12). The weights and digital photographs of tumors harvested from mice after different treatments were consistent with the tumor growth curves (Figure 5C). No clear changes in the body weights of mice were observed during 12 days post-treatment (Figure 5D). As shown in Figure 5E, both the Pt−Pd NFs+E and Pt−Pd@DON+E groups showed more efficient therapeutic effects than hose of the other formulations according to the increased dead cell cavities in H&E stained tissues, the lower percentage of Ki67-positive cells, and the stronger apoptotic markers in the TUNEL stained images. Moreover, the Pt−Pd@DON+E group showed even more potent effect on tumor cell killing than that of other groups, which was strong evidence for its synergistic tumor therapeutic effects. Routinely, there were no pathological changes in the major organs of mice receiving different treatments, indicating the *in vivo* safety of the application of each formulation (Figure S13).

In order to further understand the potential mechanism of the Pt−Pd@DON+E-induced antitumor immune response in BALB/c mice, the infiltration of $CD8^+$ T cells was first evaluated by flow cytometry (Figure 6A). Numerous studies have reported that an excellent ICD effect plays an important role in promoting the intratumoral infiltration of $CD8^+$ T cells.[40] Encouraged by the high population of mature DCs presenting antigen to T lymphocytes, 10.4 and 11.5% of $CD8^+$ T cells were respectively activated in the Pt NPs+E and Pt−Pd NFs+E groups, appreciably higher than that in the PBS group (0.45%), which may be due to the EDT-induced ICD effect. In addition, the expression of hypoxia-inducible factor 1-alpha (HIF-1$\alpha$) was significantly reduced in the Pt NPs+E and Pt−Pd NFs+E groups due to the catalase-like and peroxidase-like activities of Pt (Figure S14),[41] avoiding the exclusion of $CD8^+$ T cells in the hypoxic tumor tissues.[42] Furthermore, significant improvement of $CD8^+$ T cell (purple fluorescence) infiltration was observed in tumor tissues from mice receiving EDT treatment (Pt NPs+E and Pt−Pd NFs+E), fully demonstrating that the self-supply of $O_2$ by the Pt metal synergized with ROS-mediated EDT could elicit a strong protective immune response *via* increasing $CD8^+$ T cell infiltration in the tumor microenvironment (Figure 6C). Excitingly, Pt−Pd@DON+E activated the rate of $CD8^+$ T cells up to 23.2%, which was about 2-fold more efficient than that of the Pt NPs+E and Pt−Pd NFs+E groups, indicating that the metabolic inhibition combined with EDT resulted in synergistic immune response capabilities. To further validate whether the ROS-mediated EDT and metabolic inhibitor can directly modulate the inflammatory phenotype of macrophages in the tumor microenvironment, we have also examined the presence of M1 and M2 tumor-associated macrophages (TAMs) in the tumor tissues. Both the Pt−Pd NFs+E and Pt−Pd@DON+E groups displayed effective M1-like polarization of TAMs as detected by flow cytometry (Figure 6B). In particular, the proportion of M1 phenotype macrophages in the Pt−Pd@DON+E group was 10.9%, which was 5-fold higher than that of the Pt−Pd NFs+E group. This might be explained by the fact that DON could reduce intratumoral glutamate levels by inhibiting the hexosamide pathway. However, the regulation of the tumor immune microenvironment by Pt−Pd@DON+E was further evaluated by immunofluorescence staining assay using the typical biomarkers (Figure 6C). Electronic field alone (E) rarely caused any significant improvement of tumor-suppressive immune cells (M1-TAMs and $CD8^+$ T cells); meanwhile, EDT alone (Pt NPs+E and Pt−Pd NFs+E) only raised restricted populations, which was the main cause of tumor recurrence. Notably, the combination therapeutics with the glutamine inhibitor (Pt−Pd@DON+E) observably strengthened the infiltration of tumor-suppressive $CD8^+$ T cells and M1-like TAMs in tumor tissues, while causing the apparent downregulation of tumorigenic M2-TAMs. As shown in the Western blot experiment (Figure 6E), the expression of ICD indicators CRT and HMGB1 in tumor tissues collected from mice treated with Pt−Pd@DON+E and Pt−Pd NFs were much higher than those treated with Pt NPs and PBS. This is consistent with the results of the immune histochemical data above, fully evidencing the great ICD potential of EDT-dependent therapeutics. Moreover, a similar trend was found in the CD8 expression, which further demonstrated that the combination therapeutics with glutamine inhibitor (Pt−Pd@DON+E) could strengthen the protective immune responses against tumor challenge. The results have illuminated that EDT and glutamine inhibitor could perform synergetic immune activation in the tumor microenvironment by promoting $CD8^+$ T cell infiltration and M1-phynotype TAMs polarization.

Induction of the systemic immune response was further evaluated by measuring the serum concentrations of proinflammatory cytokines level, including interleukin 12 (IL-12p40), tumor necrosis factor $\alpha$ (TNF-$\alpha$), interferon-$\gamma$ (IFN-$\gamma$), and interleukin 6 (IL-6). Interleukins play an important role in the expression and regulation of immune response.[43] DCs are inseparable from IL-12 and IL-6, which can promote the maturation of DCs or the polarization of M2 to M1 (Figure S15).[44] Besides, TNF-$\alpha$ and IFN-$\gamma$ are critical markers for cellular immunity and play critical roles in tumor immunotherapy.[45] As ELISA assay results show in Figure 6D, the significant increase of IL-12p70 indicated more mature DCs in the Pt−Pd@DON+E group than others, and the significant upregulation of IFN-$\gamma$ levels further proved that the protective immune response was aroused by Pt−Pd@DON+E treatment.

According to published research, the poorly immunogenic 4T1 tumor model is highly metastatic to other organs, such as livers and lungs.[46] Conventional therapies are not able to inhibit the growth of distant-spread tumors and fail to prevent tumor metastasis, which are the ultimate causes of cancer deaths.[47] To further investigate immunotherapy efficacy against the metastatic formation, $1 \times 10^4$ 4T1 cells were intravenously injected into mice at 4 days post-treatment to construct metastatic models. The mice were then sacrificed at 11 days and related tissues (lungs and livers) were harvested for H&E staining investigation (Figure 6F). Obvious neutrophil infiltration and thickened alveolar walls were observed in the lung tissues of groups treated with PBS, E, Pt NPs+E, and Pt−Pd NFs+E. In contrast, lung tissue from the


https://doi.org/10.1021/acsnano.1c08544
ACS Nano XXXX, XXX, XXX−XXX

Pt−Pd@DON+E group did not show any abnormal features compared to healthy H&E-stained slices. Liver tissues showed similar trends, that is, Pt NPs+E and Pt−Pd NFs+E treatment caused decreased neutrophil infiltration compared with that of the PBS and E groups, proved that that EDT alone displayed inhibition effects of metastasis to a certain extent. More excitingly, the Pt−Pd@DON+E group showed a much better effect of inhibiting metastasis that there was almost no neutrophil infiltration in liver tissue after combined application of the glutamine inhibitor DON (Figure 6G). Therefore, the Pt−Pd@DON+E group showed much less metastasis of breast cancer to the liver and lung, ascribed to the synergistic immuno-activation by EDT in combination with glutamine inhibition.

## CONCLUSION

In this study, we have explored an advanced therapeutic platform, Pt−Pd@DON, to synergistically work against solid tumors and metastasis by performing electro-driven EDT for directly tumor killing and glutamine metabolic inhibition for antitumor immune response. Composite Pt−Pd NFs catalyzed $H_2O$ to produce supervirulent ·OH for EDT under a square-wave current, ultimately killing tumor cells and inducing ICD effects. Meanwhile, the combination with glutamine antagonist DON could subsequently enhance the protective immune response motivated by EDT *via* DCs maturation and $CD8^+$ T cell recruitment. Great achievements have been made in 4T1 tumor-bearing mice for tumor ablation and antimetastasis after Pt−Pd@DON+E treatment. This work has shown an effective tumor destruction strategy with few side effects and appeared to be rather effective at treating tumors with large sizes, which facilitates clinical development.

## EXPERIMENTAL SECTION

**Materials.** Methylene blue (MB), chloroplatinic acid hexahydrate ($H_2PtCl_6·6H_2O$), ascorbic acid (AA, 99%), potassium bromide (KBr, 99%), Pluronic F-127, sodium tetrachloropalladate (II) ($Na_2PdCl_4$, 98%), rhodamine B (tetraethyl rhodamine), and 3-(4,5-dimethylthiazol-2-yl)-2,5-diphenyltetrazolium bromide (MTT, 97%) were acquired from Aladdin. 2′-(4-Ethoxyphenyl)-5-(4-methyl-1-piperazinyl)-2,5′-bi-1*H*-benzimidazole trihydrochloride bisbenzimide (Hoechst 33342, 98%) and 2′,7′-dichlorofluorescein diacetate (DCFH-DA, 97%) were purchased from Solarbio. The Annexin V-FITC/Propidium iodide (PI) apoptosis detection kit and mitochondrial membrane potential assay kit with JC-1 were obtained from Beyotime Biotechnology. The Calcein-AM/PI Double Stain Kit was obtained from YESEN Biotechnology. Anti-calreticulin antibody, anti-HMGB1 antibody, anti-HMGB1 antibody, anti-iNOS antibody, and anti-CD8 antibody were purchased from Abcam. The anti-CD206 antibody was purchased from Proteintech. Other antibodies were purchased from eBioscience and Biolegend.

**Preparation of Pt and Pd Precursors.** Pt or Pd precursors (Pt or Pd NPs) were synthesized following a one-pot method. Briefly, 1 g of KBr and 100 mg of Pluronic F127 were put in 10 mL of water at 70 °C until they dissolved completely. Then, $H_2PtCl_6·6H_2O$ (20 mg/mL, 3.75 mL) or $Na_2PdCl_4$ (20 mg/mL, 3.75 mL) solution and ascorbic acid (AA) solution (25 mg/mL, 10 mL) were added. The reaction mixture was stirred for 12 h at 70 °C. Finally, the Pt or Pd NPs were collected by ultrafiltration centrifugation and washed three times with DI water and ethanol (1:1) to remove the residual Pluronic F127.

**Preparation of Pt−Pd NFs.** Briefly, the Pt NPs stock solution (2 mg/mL, 1 mL) and Pd NPs stock solution (0.5 mg/mL, 1 mL) were mixed and reacted overnight under magnetic agitation. Finally, the Pt−Pd NFs were collected by ultrafiltration centrifugation and washed three times with DI water and ethanol (1:1) to remove unreacted Pt or Pd NPs.

Pt−Pd NFs conjugated with the rhodamine B (RhB@ Pt−Pd NFs) probe were prepared for cellular uptake *in vitro*. First, 5 mL of Pt−Pd NFs stock solution and 1 mg of RhB probe were stirred overnight. DON loaded on Pt−Pd NFs were prepared by a simple method (Pt−Pd@DON). First, 1 mL of Pt−Pd NFs concentrated stock solution (Pt: 20 mg/mL) and 50 μg of DON were stirred overnight. Then the mix was put into a dialysis bag (MWCO: 3500 Da) to remove the excess dye.

**Electrocatalytic Activity Studies.** The degradation rates of methylene blue (MB) were used to detect the electrocatalytic properties of Pt−Pd NFs with a function signal generator. The experimental instruments are shown in Figure 2A. Briefly, different amounts of Pt−Pd NFs were added to 2 mL of PBS containing 30 μM MB in the middle well. The function signal generator, a multimeter and Pt electrodes were connected in turn. A 10 mHz square-wave electrical signal with different voltage was applied. After powering on for a different period, 30 μL of mixture was collected and diluted with PBS to 330 μL. Then the absorbance spectra of MB were characterized by UV−vis spectroscopy.

**Cell Lines and Animals.** The 4T1 breast tumor cells and 4T1 breast tumor cells were cultured in RPMI 1640, supplemented with 10% FBS and pen/strep. Cells were cultured at 37 °C and 5.0% $CO_2$.

BALB/c female mice in a weight range of 20−25 g (6−8 weeks old) were purchased from the Animal Experiment Center of Southern Medical University at Guangzhou. All animal experiments were carried out under the guidelines evaluated and approved by the ethics committee of Southern Medical University, PR China.

**Cell Internalization Assay.** To evaluate Pt−Pd NFs intracellular uptake *in vitro*, we used CLSM and flow cytometry. 4T1 breast tumor cells were exposed to RhB-loaded Pt−Pd nanoflower for different durations (2, 4, and 8 h) and then rinsed thrice with PBS. CLSM was carried out after 4T1 breast tumor cells were stained with lysosome-FITC and DAPI.

**Cell Viability Assays.** MTT assays were used to evaluate cytotoxicity *in vitro*. Briefly, 4T1 breast tumor cells were seeded onto 96-well plates at 5000 cells/well and treated with different various formulations (Pt NPs, Pt−Pd NFs, and Pt−Pd@DON) at different concentrations (Pt: 10, 20, 40, 80, and 100 μg/mL; Pd: 2, 4, 8, 16, and 20 μg/mL; DON: 12, 24, 48, 96, and 120 nM) for 24 h. Next, 10 μL of 5 mg/mL MTT was then added into each well and incubated for 4 h. Then, 150 μL of DMSO was added into each well to dissolve the resulting formazan, and the absorbance was read at 490/570 nm using a microplate reader.

For EDT treatment, 4T1 cells were plated in 24-well plates and incubated with different formulations, including PBS, E, Pt NPs, Pt NPs+E, Pt−Pd NFs, and Pt−Pd NFs+E (Pt: 100 μg/mL). After 4 h, 4T1 cells were treated with EDT therapy under a square-wave AC electric field (10 mHz, 100 s) at 2 or 5 mA for 5 min. Then, cells were replaced with fresh complete medium and incubated for another 12 h before the MTT assay.

**Detection of EDT-based ROS *In Vitro*.** DCFHDA was used to evaluate the ROS production. ROS levels were quantified by CLSM. All experimental operations are similar to EDT treatment, but there is a little difference: 4T1 breast tumor cells on 24-well plates were treated with different formulations (PBS, E, Pt NPs, Pt NPs+E, Pt−Pd NFs, and Pt−Pd NFs+E). The DCFHDA probe was added 30 min before EDT treatment. After 4 h, 4T1 cells were treated with EDT therapy under a square-wave AC electric field (10 mHz, 100 s) at 5 mA for 5 min. Subsequently, cells were instantly stained with DAPI for CLSM.

**Mitochondrial Membrane Potential Assay.** All experimental operations are similar to EDT treatment. 4T1 breast tumor cells on 24-well plates were treated with different formulations (PBS, E, Pt NPs, Pt NPs+E, Pt−Pd NFs, Pt−Pd NFs+E, Pt−Pd@DON, and Pt−Pd@DON+E). After 4 h, 4T1 cells were treated with EDT therapy under a square-wave AC electric field (10 mHz, 100 s) at 5 mA for 5 min. Next, we used mitochondrial membrane potential assay kit with JC-1 from Beyotime Biotechnology to detect the change.

***In Vitro* Studies on Tumor Cells.** All operations are the same as above. There were a few differences. 4T1 breast tumor cells on 24-


https://doi.org/10.1021/acsnano.1c08544
ACS Nano XXXX, XXX, XXX−XXX

well plates were treated with different formulations (PBS, E, Pt NPs, Pt NPs+E, Pt−Pd NFs, Pt−Pd NFs+E, Pt−Pd@DON, and Pt−Pd@DON+E). After 4 h, 4T1 cells were treated with EDT therapy under a square-wave AC electric field (10 mHz, 100 s) at 5 mA for 5 min. Two commercial assay kits (Annexin V-FITC/PI apoptosis detection kit and Calcein-AM/PI double stain kit) were used to evaluate the ability to kill tumor cells.

**Immunofluorescence Staining of ICD Markers *In Vitro*.** 4T1 cells were plated in 24-well plates and incubated with different formulations, including PBS, E, Pt NPs+E, Pt−Pd NFs+E, and Pt−Pd@DON+E (Pt: 100 $\mu$g/mL). After 4 h, 4T1 cells were treated with EDT therapy under a square-wave AC electric field (10 mHz, 100 s) at 5 mA for 5 min. Next, 4T1 cells were incubated with appropriate primary antibodies (CRT and HMGB1) and secondary antibodies conjugated with fluorescence probe, which is carried out in strict accordance with the instructions. Finally, 4T1 cells were stained with DAPI for CLSM.

***In Vivo* Electrodynamic Therapy.** To build the tumor-bearing mice, 4 or 5 weeks old female BALB/c mice were subcutaneously inoculated with 50 $\mu$L of PBS of 4T1 cells. When the tumor volume reached ~500 mm$^3$, 4T1 breast tumor cells tumor-bearing BALB/c mice were divided into 5 groups and intratumorally treated with PBS, E, Pt NPs+E, Pt−Pd NFs+E, and Pt−Pd@DON+E (Pt at 2 mg/kg, DON at 1 mg/kg, 50 $\mu$L). After 10 min, these mice were subjected to EDT treatment. In this experiment, body weights and tumor volumes were recorded monitored for 12 days. Tumor volume was calculated using the equation: (tumor length) × (tumor width)$^2$/2. After 3 days of treatment, the mice of the Pt−Pd@DON+E group were given a second tumor incubation in tumor cell challenge experiments. At 2 days after surgery (~200 mm$^3$), the mice of the Pt−Pd@DON+E group received treatment in tumor cut experiments. The mice were then sacrificed, and the tumors were harvested for H&E and immunohistochemical staining carried out by Servicebio Biological Technology and ELISA assay conducted by Jiangsu Jingmei Biotechnology Co., Ltd., Yancheng, China.

***Ex Vivo* Flow Cytometry Analysis of Immune-related Markers.** At 12 days after treatment in each group, tumor-draining lymph nodes were collected and homogenized within PBS (pH 7.4) to obtain single-cell suspensions. Cells were first stained with live/dead staining, then stained with the corresponding antibodies with the purpose of detecting the maturation of DCs: anti-CD11c-VF450, anti-CD80-FITC, and anti-CD86-PE. In order to count cytotoxic T lymphocytes in the tumor-draining lymph nodes, Gating was first carried out to exclude the dead cells and adhesive cells. CD3$^+$ cells were further gated as CD3$^+$CD45$^+$; CD8$^+$ T cells were gated as CD3$^+$CD8$^+$. Tumor slices were collected and homogenized within PBS (pH 7.4) to obtain single-cell suspensions after treatment. Cells were first stained with live/dead staining, followed by the corresponding antibodies: anti-CD11b-PC7, anti-F4/80-BV421, anti-CD86-PE, and anti-CD206-AF647. Subsequently, single-cell suspensions were analyzed on a FACScan flow cytometer.

**Western Blot Analysis.** After treatment, tumor tissues were collected from 4T1 breast tumor cells tumor-bearing BALB/c mice. We analyzed various important marks by Western blotting for CRT, HMGB1, CD8, and GAPDH.

**Statistical Analysis.** Statistical analysis was carried out on GraphPad Prism 7.0 software. Data values were illustrated as mean ± standard deviation. Statistical significance was analyzed by student's *t* test or one-way analysis of variance (ANOVA). In the figure, *, $P < 0.05$, **, $P < 0.01$, and ***, $P < 0.001$.

## ASSOCIATED CONTENT

### Supporting Information

The Supporting Information is available free of charge at https://pubs.acs.org/doi/10.1021/acsnano.1c08544.

Size distribution and long-term stability of Pt NPs and Pd NPs; UV−vis absorption spectra of MB after electrocatalytic activity studies; results of RhB-labeled Pt−Pd NFs cellular uptake detected by flow cytometer analysis and CLSM observation; mitochondrial membrane potential detection; photographs of operational procedures for EDT; H&E analysis; immunohistochemical analysis for HMGB1 and HIF-1$\alpha$; representative photos of mice at different time points after treatment; ELISA analysis of cytokines (PDF)

## AUTHOR INFORMATION


### Corresponding Authors

**Xing-Jie Liang** − *CAS Key Laboratory for Biomedical Effects of Nanomaterials and Nanosafety, CAS Center for Excellence in Nanoscience, National Center for Nanoscience and Technology of China, Beijing 100190, PR China;* orcid.org/0000-0002-4793-1705; Email: liangxj@nanoctr.cn

**Zhiqiang Yu** − *Guangdong Provincial Key Laboratory of New Drug Screening, School of Pharmaceutical Sciences, Southern Medical University, Guangzhou 510515, PR China;* orcid.org/0000-0002-1688-5558; Email: yuzq@smu.edu.cn

**Meng Yu** − *Guangdong Provincial Key Laboratory of New Drug Screening, School of Pharmaceutical Sciences, Southern Medical University, Guangzhou 510515, PR China;* orcid.org/0000-0003-1039-9687; Email: yumeng999@smu.edu.cn

### Authors

**Gui Chen** − *Guangdong Provincial Key Laboratory of New Drug Screening, School of Pharmaceutical Sciences, Southern Medical University, Guangzhou 510515, PR China*

**Qing Xu** − *Guangdong Provincial Key Laboratory of New Drug Screening, School of Pharmaceutical Sciences, Southern Medical University, Guangzhou 510515, PR China*

**Zhenzhen Feng** − *Guangdong Provincial Key Laboratory of New Drug Screening, School of Pharmaceutical Sciences, Southern Medical University, Guangzhou 510515, PR China*

**Qinqin Xu** − *Guangdong Provincial Key Laboratory of New Drug Screening, School of Pharmaceutical Sciences, Southern Medical University, Guangzhou 510515, PR China*

**Xuhui Zhang** − *The First Clinical Medical School, Southern Medical University, Guangzhou 510515, PR China*

**Yuanyuan Yang** − *Guangdong Provincial Key Laboratory of New Drug Screening, School of Pharmaceutical Sciences, Southern Medical University, Guangzhou 510515, PR China*

**Yuxuan Zhang** − *CAS Key Laboratory for Biomedical Effects of Nanomaterials and Nanosafety, CAS Center for Excellence in Nanoscience, National Center for Nanoscience and Technology of China, Beijing 100190, PR China*

Complete contact information is available at: https://pubs.acs.org/10.1021/acsnano.1c08544

### Author Contributions

‖G.C. and Q.X. contributed equally to this work.


### Notes

The authors declare no competing financial interest.

## ACKNOWLEDGMENTS

This research was financially supported by GDNRC [Guangdong Nature Resource Center] (2020) 037, the National Natural Science Foundation of China (81773642 and 52073139), the Natural Science Foundation of Guangdong Province (2019A1515011619 and 2019A1515011498),

the Key Laboratory of Biomedical Effects of Nanomaterials and Nanosafety, National Center for Nanoscience and Technology, CAS (NSKF201819), and the Government of the Russian Federation (Megagrant, 2020-220-08-5262).

## REFERENCES

(1) Chong, S. J. F.; Iskandar, K.; Lai, J. X. H.; Qu, J.; Raman, D.; Valentin, R.; Herbaux, C.; Collins, M.; Low, I. C. C.; Loh, T.; Davids, M.; Pervaiz, S. Serine-70 Phosphorylated Bcl-2 Prevents Oxidative Stress-Induced DNA Damage by Modulating the Mitochondrial Redox Metabolism. *Nucleic Acids Res.* **2020**, *48*, 12727−12745.

(2) Wang, K.; Ma, W.; Xu, Y.; Liu, X.; Chen, G.; Yu, M.; Pan, Q.; Huang, C.; Li, X.; Mu, Q.; Sun, Y.; Yu, Z. Design of a Novel Mitochondria Targetable Turn-On Fluorescence Probe for Hydrogen Peroxide and Its Two-Photon Bioimaging Applications. *Chin. Chem. Lett.* **2020**, *31*, 3149−3152.

(3) Thomson, G. J.; Hernon, C.; Austriaco, N.; Shapiro, R. S.; Belenky, P.; Bennett, R. J. Metabolism-Induced Oxidative Stress and DNA Damage Selectively Trigger Genome Instability in Polyploid Fungal Cells. *Eur. Mol. Biol. Organ. J.* **2019**, *38*, 101597−101613.

(4) Anderson, A. P.; Luo, X.; Russell, W.; Yin, Y. W. Oxidative Damage Diminishes Mitochondrial DNA Polymerase Replication Fidelity. *Nucleic Acids Res.* **2020**, *48*, 817−829.

(5) Yuan, B.; Wu, H.; Wang, H.; Tang, B.; Xu, J. F.; Zhang, X. A Self-Degradable Supramolecular Photosensitizer with High Photodynamic Therapeutic Efficiency and Improved Safety. *Angew. Chem., Int. Ed. Engl.* **2021**, *60*, 706−710.

(6) Li, L.; Yang, Z.; Fan, W.; He, L.; Cui, C.; Zou, J.; Tang, W.; Jacobson, O.; Wang, Z.; Niu, G.; Hu, S.; Chen, X. *In Situ* Polymerized Hollow Mesoporous Organosilica Biocatalysis Nanoreactor for Enhancing Ros-Mediated Anticancer Therapy. *Adv. Funct. Mater.* **2020**, *30*, 1907716−1907726.

(7) Hao, Y.; Chen, Y.; He, X.; Yu, Y.; Han, R.; Li, Y.; Yang, C.; Hu, D.; Qian, Z. Polymeric Nanoparticles with Ros-Responsive Prodrug and Platinum Nanozyme for Enhanced Chemophotodynamic Therapy of Colon Cancer. *Adv. Sci.* **2020**, *7*, 2001853−2001866.

(8) Gong, F.; Cheng, L.; Yang, N.; Gong, Y.; Ni, Y.; Bai, S.; Wang, X.; Chen, M.; Chen, Q.; Liu, Z. Preparation of $Tih_{1.924}$ Nanodots by Liquid-Phase Exfoliation for Enhanced Sonodynamic Cancer Therapy. *Nat. Commun.* **2020**, *11*, 3712−3722.

(9) Zhou, R.; Liu, X.; Wu, Y.; Xiang, H.; Cao, J.; Li, Y.; Yin, W.; Zu, Y.; Li, J.; Liu, R.; Zhao, F.; Liu, Z.; Chen, C.; Gu, Z.; Yan, L.; Zhao, Y. Suppressing the Radiation-Induced Corrosion of Bismuth Nanoparticles for Enhanced Synergistic Cancer Radiophototherapy. *ACS Nano* **2020**, *14*, 13016−13029.

(10) Ni, K.; Lan, G.; Song, Y.; Hao, Z.; Lin, W. Biomimetic Nanoscale Metal-Organic Framework Harnesses Hypoxia for Effective Cancer Radiotherapy and Immunotherapy. *Chem. Sci.* **2020**, *11*, 7641−7653.

(11) Gu, T.; Wang, Y.; Lu, Y.; Cheng, L.; Feng, L.; Zhang, H.; Li, X.; Han, G.; Liu, Z. Platinum Nanoparticles to Enable Electrodynamic Therapy for Effective Cancer Treatment. *Adv. Mater.* **2019**, *31*, 1806803−1806811.

(12) Pedone, D.; Moglianetti, M.; De Luca, E.; Bardi, G.; Pompa, P. P. Platinum Nanoparticles in Nanobiomedicine. *Chem. Soc. Rev.* **2017**, *46*, 4951−4975.

(13) Li, W.; Yang, J.; Luo, L.; Jiang, M.; Qin, B.; Yin, H.; Zhu, C.; Yuan, X.; Zhang, J.; Luo, Z.; et al. Targeting Photodynamic and Photothermal Therapy to the Endoplasmic Reticulum Enhances Immunogenic Cancer Cell Death. *Nat. Commun.* **2019**, *10*, 3349−3364.

(14) Chen, S.; Li, D.; Du, X.; He, X.; Huang, M.; Wang, Y.; Yang, X.; Wang, J. Carrier-Free Nanoassembly of Doxorubicin Prodrug and Sirna for Combinationally Inducing Immunogenic Cell Death and Reversing Immunosuppression. *Nano Today* **2020**, *35*, 100924−100933.

(15) Wang, H.; Wang, K.; He, L.; Liu, Y.; Dong, H.; Li, Y. Engineering Antigen as Photosensitiser Nanocarrier to Facilitate Ros Triggered Immune Cascade for Photodynamic Immunotherapy. *Biomaterials* **2020**, *244*, 119964−119977.

(16) Ding, B.; Zheng, P.; Jiang, F.; Zhao, Y.; Wang, M.; Chang, M.; Ma, P.; Lin, J. $MnO_X$ Nanospikes as Nanoadjuvants and Immunogenic Cell Death Drugs with Enhanced Antitumor Immunity and Antimetastatic Effect. *Angew. Chem., Int. Ed. Engl.* **2020**, *59*, 16381−16384.

(17) Ni, K.; Luo, T.; Nash, G. T.; Lin, W. Nanoscale Metal-Organic Frameworks for Cancer Immunotherapy. *Acc. Chem. Res.* **2020**, *53*, 1739−1748.

(18) Huang, Z.; Wang, Y.; Yao, D.; Wu, J.; Hu, Y.; Yuan, A. Nanoscale Coordination Polymers Induce Immunogenic Cell Death by Amplifying Radiation Therapy Mediated Oxidative Stress. *Nat. Commun.* **2021**, *12*, 145−162.

(19) Yu, Z.; Guo, J.; Hu, M.; Gao, Y.; Huang, L. Icaritin Exacerbates Mitophagy and Synergizes with Doxorubicin to Induce Immunogenic Cell Death in Hepatocellular Carcinoma. *ACS Nano* **2020**, *14*, 4816−4828.

(20) Hossain, D. M. S.; Javaid, S.; Cai, M.; Zhang, C.; Sawant, A.; Hinton, M.; Sathe, M.; Grein, J.; Blumenschein, W.; Pinheiro, E. M.; Chackerian, A. Dinaciclib Induces Immunogenic Cell Death and Enhances Anti-PD1-Mediated Tumor Suppression. *J. Clin. Invest.* **2018**, *128*, 644−654.

(21) Lu, Z.; Gao, J.; Fang, C.; Zhou, Y.; Li, X.; Han, G. Porous Pt Nanospheres Incorporated with GOx to Enable Synergistic Oxygen-Inductive Starvation/Electrodynamic Tumor Therapy. *Adv. Sci.* **2020**, *7*, 2001223−2001231.

(22) Chen, T.; Gu, T.; Cheng, L.; Li, X.; Han, G.; Liu, Z. Porous Pt Nanoparticles Loaded with Doxorubicin to Enable Synergistic Chemo-/Electrodynamic Therapy. *Biomaterials* **2020**, *255*, 120202−120212.

(23) Jeong, S. D.; Jung, B. K.; Ahn, H. M.; Lee, D.; Ha, J.; Noh, I.; Yun, C. O.; Kim, Y. C. Immunogenic Cell Death Inducing Fluorinated Mitochondria-Disrupting Helical Polypeptide Synergizes with PDL1 Immune Checkpoint Blockade. *Adv. Sci.* **2021**, *8*, 2001308−2001320.

(24) Feng, B.; Zhou, F.; Hou, B.; Wang, D.; Wang, T.; Fu, Y.; Ma, Y.; Yu, H.; Li, Y. Binary Cooperative Prodrug Nanoparticles Improve Immunotherapy by Synergistically Modulating Immune Tumor Microenvironment. *Adv. Mater.* **2018**, *30*, 1803001−1803010.

(25) Agliardi, G.; Liuzzi, A. R.; Hotblack, A.; De Feo, D.; Núñez, N.; Stowe, C. L.; Friebel, E.; Nannini, F.; Rindlisbacher, L.; Roberts, T. A.; et al. Intratumoral IL-12 Delivery Empowers CAR-T Cell Immunotherapy in a Pre-Clinical Model of Glioblastoma. *Nat. Commun.* **2021**, *12*, 444−454.

(26) Yan, S.; Zeng, X.; Tang, Y.; Liu, B. F.; Wang, Y.; Liu, X. Activating Antitumor Immunity and Antimetastatic Effect through Polydopamine-Encapsulated Core-Shell Upconversion Nanoparticles. *Adv. Mater.* **2019**, *31*, 1905825−1905836.

(27) Park, S.; Pascua, E.; Lindquist, K. C.; Kimberlin, C.; Deng, X.; Mak, Y. S. L.; Melton, Z.; Johnson, T. O.; Lin, R.; Boldajipour, B.; et al. Direct Control of CAR-T Cells through Small Molecule-Regulated Antibodies. *Nat. Commun.* **2021**, *12*, 710−719.

(28) Wang, X.; Li, B.; Kim, Y. J.; Wang, Y. C.; Li, Z.; Yu, J.; Zeng, S.; Ma, X.; Choi, I. Y.; Di Biase, S.; et al. Targeting Monoamine Oxidase A for T Cell-Based Cancer Immunotherapy. *Sci. Immunol.* **2021**, *6*, abh2383.

(29) Leone, R. D.; Zhao, L.; Englert, J. M.; Sun, I. M.; Oh, M. H.; Sun, I. H.; Arwood, M. L.; Bettencourt, I. A.; Patel, C. H.; Wen, J.; Tam, A.; Blosser, R. L.; Prchalova, E.; Alt, J.; Rais, R.; Slusher, B. S.; Powell, J. D. Glutamine Blockade Induces Divergent Metabolic Programs to Overcome Tumor Immune Evasion. *Science* **2019**, *366*, 1013−1021.

(30) Zhu, X.; Nedelcovych, M. T.; Thomas, A. G.; Hasegawa, Y.; Moreno-Megui, A.; Coomer, W.; Vohra, V.; Saito, A.; Perez, G.; Wu, Y.; Alt, J.; Prchalova, E.; Tenora, L.; Majer, P.; Rais, R.; Rojas, C.; Slusher, B. S.; Kamiya, A. JHU-083 Selectively Blocks Glutaminase Activity in Brain $CD11b^+$ Cells and Prevents Depression-Associated Behaviors Induced by Chronic Social Defeat Stress. *Neuropsychopharmacology* **2019**, *44*, 683−694.



https://doi.org/10.1021/acsnano.1c08544
*ACS Nano* XXXX, XXX, XXX−XXX

(31) Tenora, L.; Alt, J.; Dash, R. P.; Gadiano, A. J.; Novotná, K.; Veeravalli, V.; Lam, J.; Kirkpatrick, Q. R.; Lemberg, K. M.; Majer, P.; Rais, R.; Slusher, B. S. Tumor-Targeted Delivery of 6-Diazo-5-Oxo-L-Norleucine (DON) Using Substituted Acetylated Lysine Prodrugs. *J. Med. Chem.* **2019**, *62*, 3524−3538.
(32) Asthana, A.; Ramakrishnan, P.; Vicioso, Y.; Zhang, K.; Parameswaran, R. Hexosamine Biosynthetic Pathway Inhibition Leads to Aml Cell Differentiation and Cell Death. *Mol. Cancer Ther.* **2018**, *17*, 2226−2237.
(33) Sharma, N. S.; Gupta, V. K.; Garrido, V. T.; Hadad, R.; Durden, B. C.; Kesh, K.; Giri, B.; Ferrantella, A.; Dudeja, V.; Saluja, A.; Banerjee, S. Targeting Tumor-Intrinsic Hexosamine Biosynthesis Sensitizes Pancreatic Cancer to Anti-PD1 Therapy. *J. Clin. Invest.* **2020**, *130*, 451−465.
(34) Qi, T.; Chen, B.; Wang, Z.; Du, H.; Liu, D.; Yin, Q.; Liu, B.; Zhang, Q.; Wang, Y. A pH-Activatable Nanoparticle for Dual-Stage Precisely Mitochondria-Targeted Photodynamic Anticancer Therapy. *Biomaterials* **2019**, *213*, 119219−119258.
(35) Deng, W.; McKelvey, K. J.; Guller, A.; Fayzullin, A.; Campbell, J. M.; Clement, S.; Habibalahi, A.; Wargocka, Z.; Liang, L.; Shen, C.; Howell, V. M.; Engel, A. F.; Goldys, E. M. Application of Mitochondrially Targeted Nanoconstructs to Neoadjuvant X-Ray-Induced Photodynamic Therapy for Rectal Cancer. *ACS Cent. Sci.* **2020**, *6*, 715−726.
(36) Chen, C.; Ni, X.; Jia, S.; Liang, Y.; Wu, X.; Kong, D.; Ding, D. Massively Evoking Immunogenic Cell Death by Focused Mitochondrial Oxidative Stress Using an AIE Luminogen with a Twisted Molecular Structure. *Adv. Mater.* **2019**, *31*, 1904914−1904924.
(37) Liu, X.; Feng, Z.; Wang, C.; Su, Q.; Song, H.; Zhang, C.; Huang, P.; Liang, X. J.; Dong, A.; Kong, D.; Wang, W. Co-Localized Delivery of Nanomedicine and Nanovaccine Augments the Postoperative Cancer Immunotherapy by Amplifying T-Cell Responses. *Biomaterials* **2020**, *230*, 119649−119664.
(38) Ho, W. J.; Jaffee, E. M. Disrupting a Converging Metabolic Target Turns up the Immunologic-Heat in Pancreatic Tumors. *J. Clin. Invest.* **2020**, *130*, 71−73.
(39) Zhou, F.; Feng, B.; Yu, H.; Wang, D.; Wang, T.; Ma, Y.; Wang, S.; Li, Y. Tumor Microenvironment-Activatable Prodrug Vesicles for Nanoenabled Cancer Chemoimmunotherapy Combining Immunogenic Cell Death Induction and CD47 Blockade. *Adv. Mater.* **2019**, *31*, 1805888−1805898.
(40) Xu, S.; Chaudhary, O.; Rodríguez-Morales, P.; Sun, X.; Chen, D.; Zappasodi, R.; Xu, Z.; Pinto, A. F. M.; Williams, A.; Schulze, I.; et al. Uptake of Oxidized Lipids by the Scavenger Receptor CD36 Promotes Lipid Peroxidation and Dysfunction in $CD8^+$ T cells in Tumors. *Immunity* **2021**, *54*, 1561.
(41) Chen, G.; Yang, Y.; Xu, Q.; Ling, M.; Lin, H.; Ma, W.; Sun, R.; Xu, Y.; Liu, X.; Li, N.; Yu, Z.; Yu, M. Self-Amplification of Tumor Oxidative Stress with Degradable Metallic Complexes for Synergistic Cascade Tumor Therapy. *Nano Lett.* **2020**, *20*, 8141−8150.
(42) Liikanen, I.; Lauhan, C.; Quon, S.; Omilusik, K.; Phan, A. T.; Bartrolí, L. B.; Ferry, A.; Goulding, J.; Chen, J.; Scott-Browne, J. P.; Yustein, J. T.; Scharping, N. E.; Witherden, D. A.; Goldrath, A. W. Hypoxia-Inducible Factor Activity Promotes Antitumor Effector Function and Tissue Residency by $CD8^+$ T Cells. *J. Clin. Invest.* **2021**, *131*, 143729−143746.
(43) Yu, M.; Duan, X.; Cai, Y.; Zhang, F.; Jiang, S.; Han, S.; Shen, J.; Shuai, X. Multifunctional Nanoregulator Reshapes Immune Microenvironment and Enhances Immune Memory for Tumor Immunotherapy. *Adv. Sci.* **2019**, *6*, 1900037−1900052.
(44) Luo, L.; Zhu, C.; Yin, H.; Jiang, M.; Zhang, J.; Qin, B.; Luo, Z.; Yuan, X.; Yang, J.; Li, W.; Du, Y.; You, J. Laser Immunotherapy in Combination with Perdurable PD1 Blocking for the Treatment of Metastatic Tumors. *ACS Nano* **2018**, *12*, 7647−7662.
(45) Liu, J.; Ai, X.; Cabral, H.; Liu, J.; Huang, Y.; Mi, P. Tumor Hypoxia-Activated Combinatorial Nanomedicine Triggers Systemic Antitumor Immunity to Effectively Eradicate Advanced Breast Cancer. *Biomaterials* **2021**, *273*, 120847−120862.
(46) Castro, F.; Pinto, M. L.; Pereira, C. L.; Serre, K.; Barbosa, M. A.; Vermaelen, K.; Gärtner, F.; Gonçalves, R. M.; De Wever, O.; Oliveira, M. J. Chitosan/γ-PGA Nanoparticles-Based Immunotherapy as Adjuvant to Radiotherapy in Breast Cancer. *Biomaterials* **2020**, *257*, 120218−120232.
(47) Chen, Q.; Chen, J.; Yang, Z.; Xu, J.; Xu, L.; Liang, C.; Han, X.; Liu, Z. Nanoparticle-Enhanced Radiotherapy to Trigger Robust Cancer Immunotherapy. *Adv. Mater.* **2019**, *31*, 1802228−1802238.




https://doi.org/10.1021/acsnano.1c08544
ACS Nano XXXX, XXX, XXX−XXX